Graphical Interface Development Based on DAQ Module and Accelerometers in Representing Ground Wave Propagation

Risky Martin Antosia, *Member, IAENG*

***Abstract*—Utilizing an embedded system is crucial for exploring various fields of study, such as ground wave propagation, which interests earth and civil engineering scientists/students. The constructed system includes a data acquisition (DAQ) module and vibration sensors, which can be employed to study wave propagation. It is particularly beneficial for students lacking access to necessary instruments. The sensors utilized are MEMS accelerometers. Developed using LabVIEW programming software, a graphical interface controls the DAQ and visualizes the wave signals. The primary parameter of the DAQ is the sampling frequency, which is adjustable by the user from 1 kHz to 25 kHz. Consequently, when testing with distances ranging from 1 to 10 m between the sensor and the source, a sampling rate exceeding 10 kHz represents ground acceleration reliably. Another aspect addressed in subsequent studies using this system involves analyzing the results to characterize ground wave attributes.**

***Index Terms*— DAQ, MEMS accelerometers, LabVIEW, wave propagation.**

I. Introduction

Typically, a visual interface within an embedded system is widely utilized for data acquisition, particularly in reading analog signals, facilitating user operation, and output signal monitoring. LabVIEW is a commonly employed interface, compatible with various data acquisition (DAQ) modules such as National Instruments (NI) DAQ [1]–[3], Measurement Computing (MC) DAQ [4], [5], or Arduino [6], [7]. Additionally, other systems integrate Matlab as graphical software with a single-board computer (SBC) [8], [9] or utilize a web-based interface with the SBC [10]. Numerous studies leverage interface software for real-time monitoring, including remote data acquisition [10]–[12], vibration analysis related to specific equipment [1], [2], [4], [13], or acceleration analysis [6], [8], [14].

Many studies focusing on vibration/acceleration analysis primarily employ accelerometers as sensors in the system. These sensors are extensively utilized in earthquake [8], [15]–[17] or structural [6], [10], [15]–[20] monitoring, seismic monitoring [20]–[23], natural resource exploration [24], [25], seismic data acquisition system [26]–[30], and ground vibration analysis [31]–[33]. Most utilize micro-electro-mechanical systems (MEMS) based accelerometers due to their compact size and lightness compared to conventional sensors like seismometers [24]. MEMS accelerometers can detect a wide range of wave frequencies [20], [24], [25], making them advantageous for ground vibration monitoring and crucial for mitigating environmental hazards near infrastructure [31]–[33]. One of its parameters can be viewed from peak-peak velocity [32] or peak-peak acceleration [31], [33].

Therefore, this study proposes building a simple measurement system to detect ground wave propagation, comprising an MC DAQ and three single capacitive MEMS accelerometers that are orthogonally assembled to represent a triaxial accelerometer sensor. MEMS sensors are chosen for their superior performance compared to other types. LabVIEW will be implemented for the graphical user interface due to its ease of software development and capability to acquire high-speed analog data. Moreover, this study can be an educational tool for explaining ground wave propagation to students through experimentation.

II. Material and Methods

The capacitive MEMS accelerometer is driven by two voltage supplies: positive and negative. Within the single MEMS device, a movable electrode or mass is positioned between two fixed plates, one above and one below. Each electrode is linked to a voltage supply, with the top electrode connected to the positive supply ($+V_0$) and the bottom to the negative supply ($-V_0$). When two metal plates are aligned facing each other and are parallel at a specific distance (d), a capacitance value is established. The internal system can be represented as a series circuit of two capacitors (C_1 and C_2). The movable mass will shift its position accordingly if particle motion is detected. Consequently, the displacement will be directly proportional to the voltage in the movable sensor. This concept is illustrated in Fig. 1.

Suppose the motion is represented by x, and the corresponding voltage output is denoted as V_x. For instance, if the movable plate detects a motion leading it to shift upwards, the distance for the top capacitor would be $d - x$, while for the bottom one, it would be $d + x$. Since these capacitors are part of the same system, their electrical charges will be equivalent. This relationship can be expressed as follows,

$$Q_1 = Q_2 \tag{1}$$

Manuscript received August 29, 2023; revised April 25, 2024.

R. M. Antosia is a lecturer at the Department of Geophysical Engineering, Faculty of Industrial Technology, Sumatera Institute of Technology, Indonesia. e-mail: martin.antosia@tg.itera.ac.id.

$$C_1V_1 = C_2V_2 \quad (2)$$

where V_1 and V_2 are potential differences in the first and second capacitors, respectively. Then, the expression will be

$$C_1(V_0 - V_x) = C_2(V_x - (-V_0)) \quad (3)$$

Since the dielectric coefficient and plate area are the same in those capacitors, then (3) will be

$$\frac{V_0 - V_x}{d - x} = \frac{V_x + V_0}{d + x} \quad (4)$$

The elucidation can be presented as follows,

$$d(V_0 - V_x) + x(V_0 - V_x) = d(V_x + V_0) - x(V_x + V_0)$$

$$x(V_0 - V_x) + x(V_x + V_0) = d(V_x + V_0) - d(V_0 - V_x)$$

$$2xV_0 = 2dV_x$$

$$V_x = \left(\frac{V_0}{d}\right)x \quad (5)$$

Hence, (5) expresses the output sensing in a capacitive MEMS sensor.

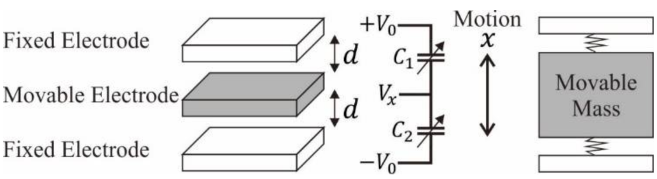

Fig. 1. A simplified diagram of capacitive MEMS accelerometer (redrawing from [34]).

The displacement of the mass sensing occurs due to an external force (F_{ext}), and within the mass plate, specific components function akin to springs (representing F_{spring}). Consequently, both Newton's and Hooke's laws are applicable, manifesting in the following manner,

$$F_{ext} = F_{spring} \quad (6)$$

$$ma = kx \quad (7)$$

$$a = \left(\frac{k}{m}\right)x \quad (8)$$

The last expression shows that the particle motion detected by the sensor is proportional to its acceleration. Thus, in the single MEMS sensor, the acceleration proportionates to the output voltage,

$$a \approx V_x \quad (9)$$

This setup utilizes a seismic-grade MEMS accelerometer, the SF1500SN model from Colibrys [24], [35], which offers superior sensitivity compared to similar options [22]. Its specifications are detailed in Table 1. Three individual MEMS sensors are arranged orthogonally within a tube casing to construct a three-axis accelerometer sensor, as its schematic is illustrated in Fig. 2(a). Power is provided to the sensor system by a 12 V DC battery, which is then converted by a DC-DC module to ±12 V to meet the supply requirements outlined in Table 1. Consequently, the maximum linear output theoretically reaches approximately ±7.2 V.

Fig. 2(b) illustrates the constructed system and the measurement approach. The DAQ module employed is of the USB-201 type, powered by +5 V through a USB connection from a computer. Its key features include eight single-ended 12-bit analog inputs, a maximum sampling rate of 100 kHz (f_{max}), and an input voltage range of ±10 V [36].

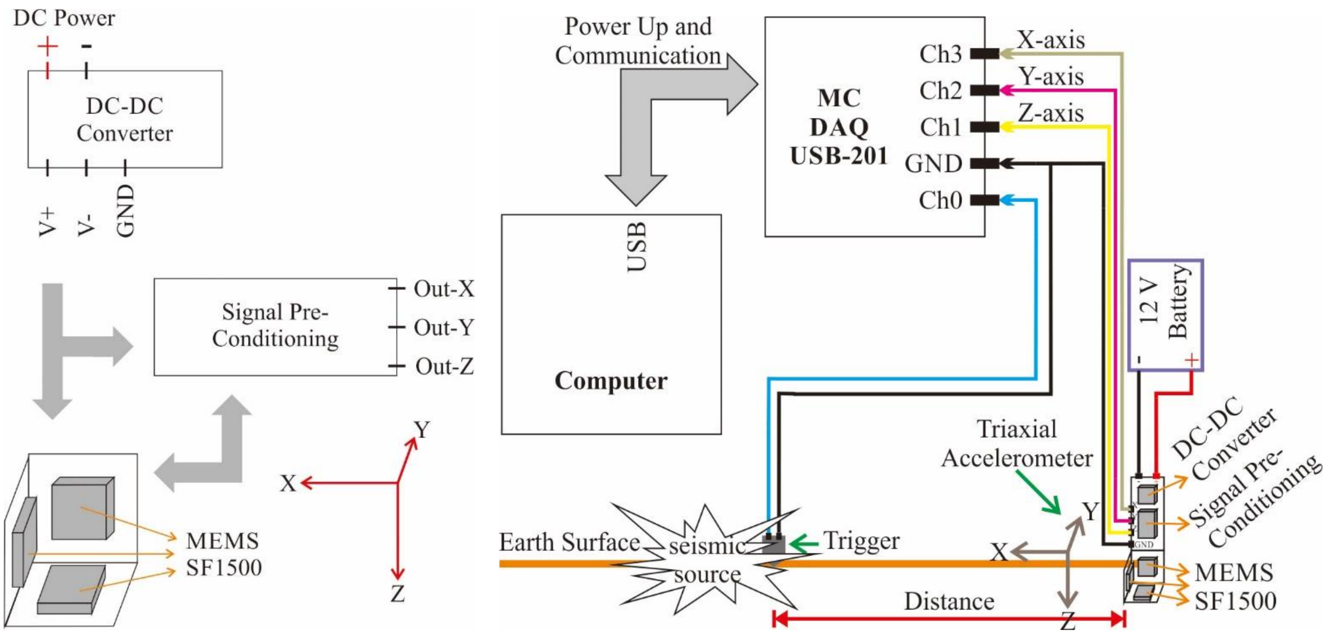

Fig. 2. System design: (a) A triaxial system based on three single MEMS accelerometers, and (b) The measurement system of ground wave propagation. (These images are based on the author's documentation and designs).

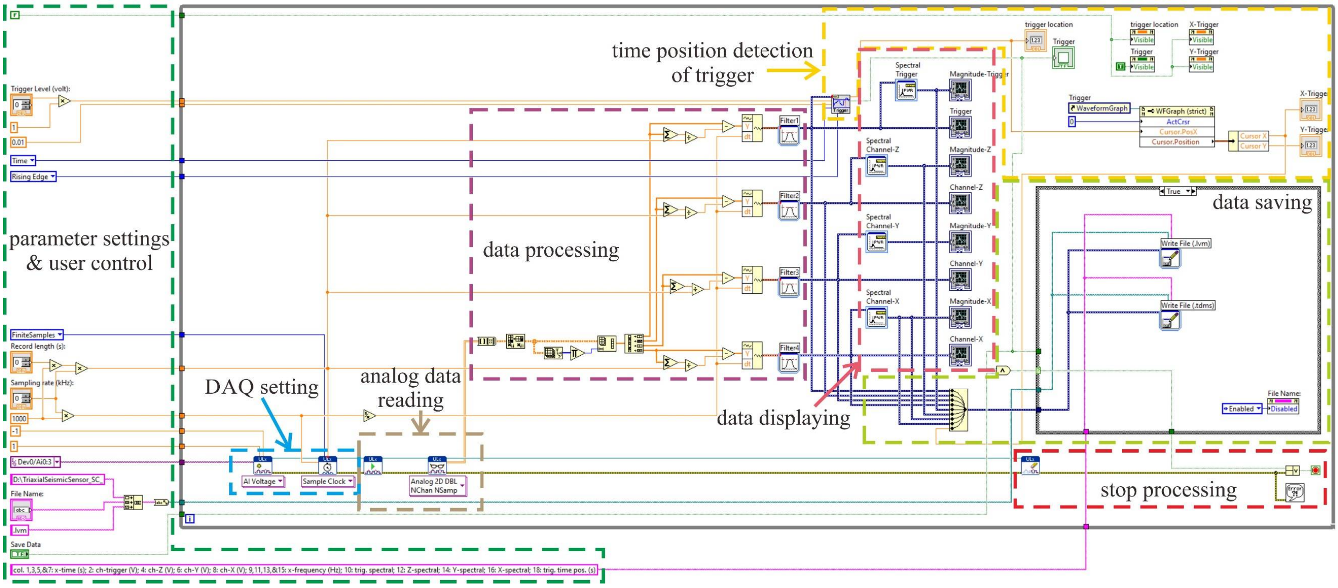

Fig. 3. The block diagram of LabVIEW.

Since the analog-to-digital signal conversion method is multiplexing, the equation below applies to each utilized input channel,

$$f_{ch} = \frac{f_{max}}{n_{ch}} \tag{10}$$

here, f_{ch} represents the sampling frequency of each channel while n_{ch} denotes the sequential number of the occupied channel. The system utilizes four input channels: one for the signal trigger (channel 0) and the remaining for the measured signals from the accelerometer sensor, allocated to the X-, Y-, and Z-axes (channels 1-3, respectively). Consequently, the maximum sampling frequency reaches 25 kHz.

TABLE 1. THE SPECIFICATION OF SF1500SN MEMS ACCELEROMETER [35].

Parameter	Unit
Voltage supply	±6 - ±15 V
Linear output range	±3 g
Sensitivity	2.4 ± 0.24 V/g
Noise	< 0.5 $\mu g_{rms}/\sqrt{Hz}$
Frequency response	DC – 1,500 Hz

As previously mentioned, the sensors' maximum voltage output, around ±7.2 V, allows for direct connection to the DAQ analog inputs. The assembled triaxial sensor is positioned on the ground surface at a specified distance from a trigger sensor to test the system. Subsequently, the seismic source is struck onto the ground near the trigger, causing all signals to be captured and displayed on the software interface.

The LabVIEW programming language is employed to operate software interfaces. Initially, parameter settings are defined, encompassing constant and adjustable variables, with user control over the latter. These variables configure the DAQ, with fixed settings determining the minimum and maximum voltage amplitudes to be read. In this instance, the author sets these values to ±1 V due to the low signal strength detected by the sensors. The adjustable parameters include the sampling frequency and record length of the DAQ. Once correctly configured, the software begins continuously reading analog input data.

Operation proceeds until the trigger channel detects the seismic wave caused by the impact source on the surface. At this point, signals from all channels (both time and frequency domains) are represented on the monitor for the trigger, X-, Y-, and Z-axes. Simultaneously, the data is saved on the computer drive, and the software halts. The software diagram is depicted in Fig. 3.

III. RESULTS AND DISCUSSION

The sensor system is positioned on the soil surface at a depth of approximately 5 cm to ensure proper coupling with the ground, as depicted in the left image of Fig. 4. The recording module, situated near the trigger, monitors the signals primarily to detect the onset of movement from the stimulus. The MEMS sensors and the trigger are positioned at 1-10 m intervals, with a spacing of 1 m, as shown on the right side of Fig. 4. Data is collected at each interval. The recorded signals at a 1 m distance between the sensors and the trigger are displayed in Figs. 5 and 6, with sampling rates of 5 kHz and 20 kHz, respectively. Despite differences in sampling rates, the signals exhibit consistent patterns. These patterns are analyzed in time series (left) and frequency domain (right). Regardless of the sampling frequency used for data acquisition (DAQ), the resulting trigger or sensor signals along the X-, Y-, and Z-axes remain consistent. The signals from each axis and sampling rate (ranging from 1 to 25 kHz) are superimposed in Fig. 7, excluding the trigger, to confirm their similarities and validate earlier assumptions. The shapes of these signals are nearly identical, except for the signal obtained at a 1 kHz sampling frequency, which displays a slight shift due to the sampling frequency itself. With a 1 kHz sampling rate, the time interval between samples is 1 ms (or 1000 µs). As the sampling frequency increases, this interval decreases accordingly, ranging from 200 to 40 µs for 5, 10, 15, 20, and 25 kHz sampling rates, respectively. Given a signal length of 0.1 s (or 100 ms), differences between intervals ranging from 200 µs to 40 µs are invisible to the human eye. However, a 1 ms interval results in noticeable motion shifts, rendering the signal distinct from others and potentially perceived as anomalous.

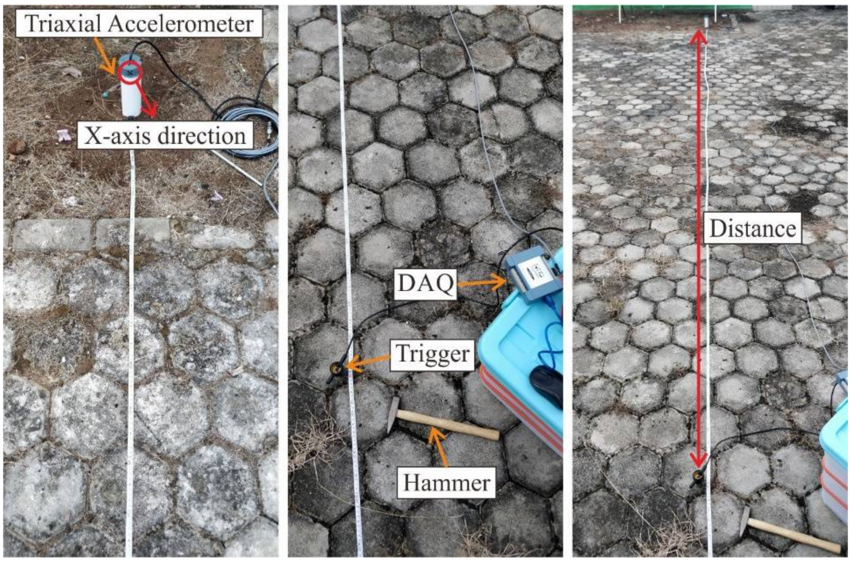

Fig. 4. The system testing, triaxial MEMS accelerometer (left), recording system (middle), and a straight line between sensors and a trigger (right).

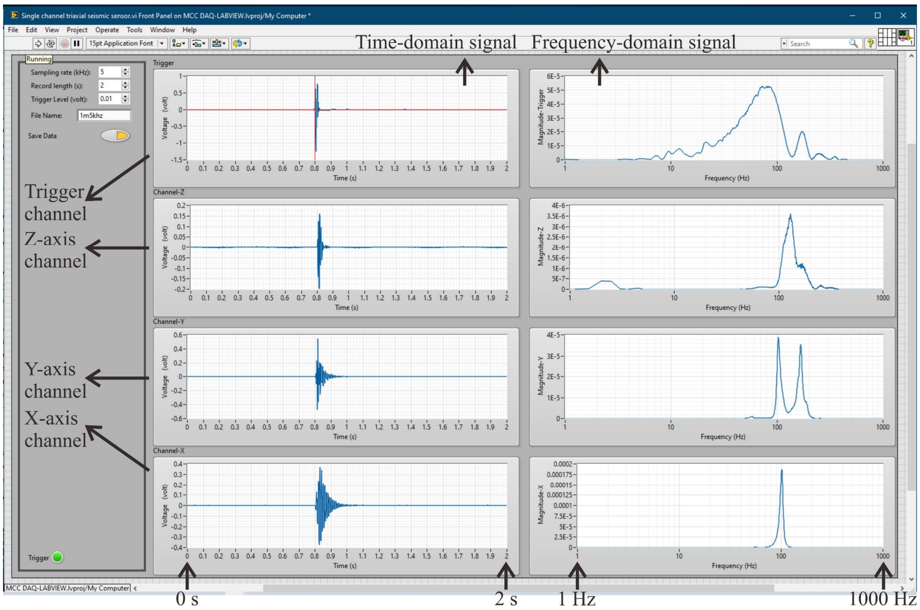

Fig. 5. Displayed signal at 5 kHz sampling rate with 1 m interval.

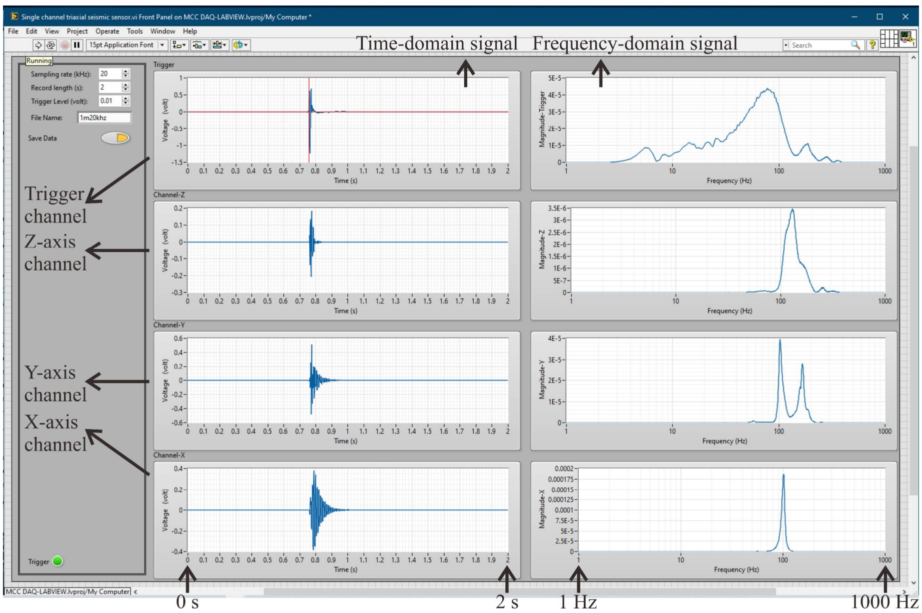

Fig. 6. Displayed signal at 20 kHz sampling rate 1 m interval.

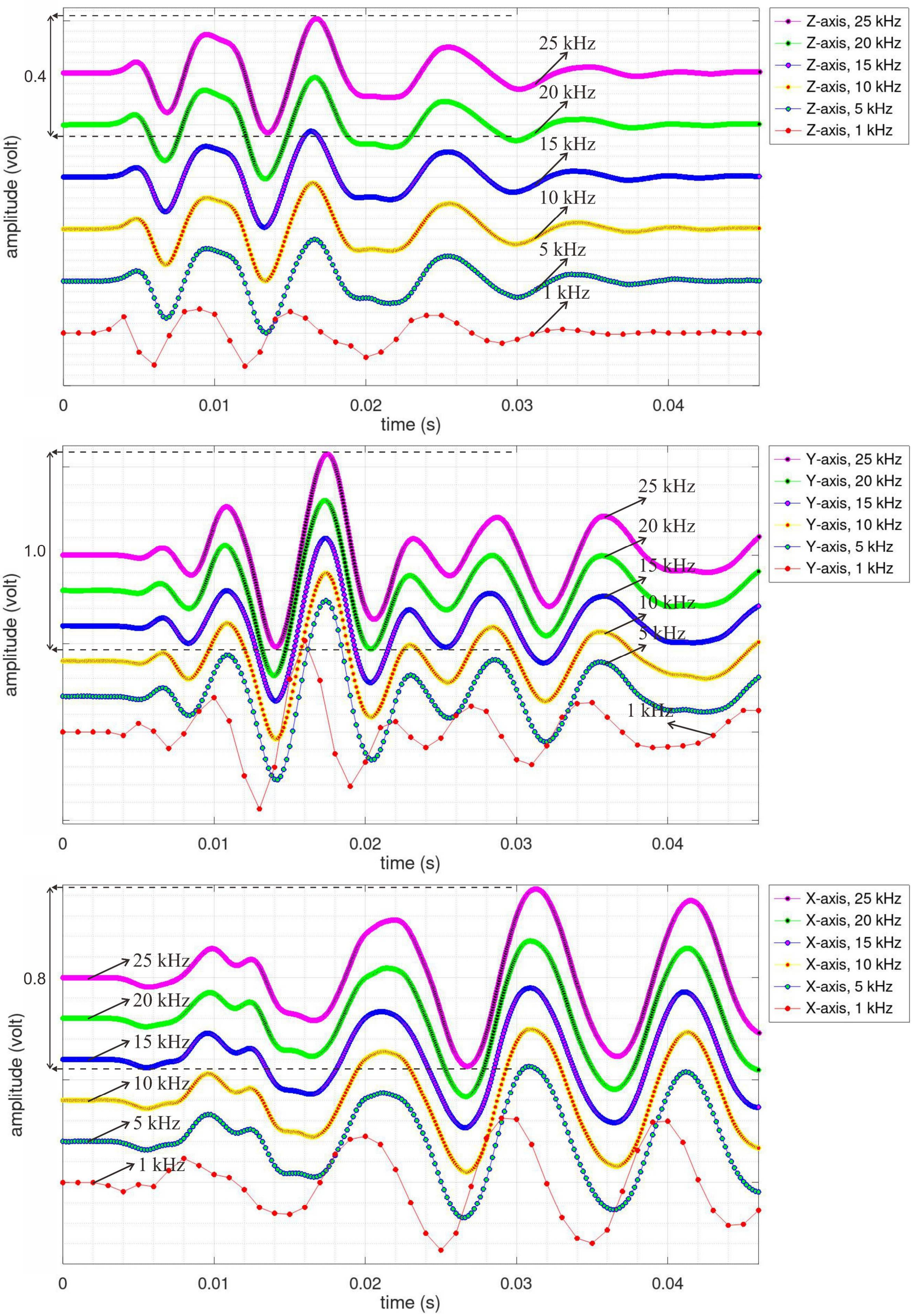

Fig. 7. Signal at a distance of 1 m with different sampling frequencies, (top) Z-axis, (middle) Y-axis, and (bottom) X-axis.

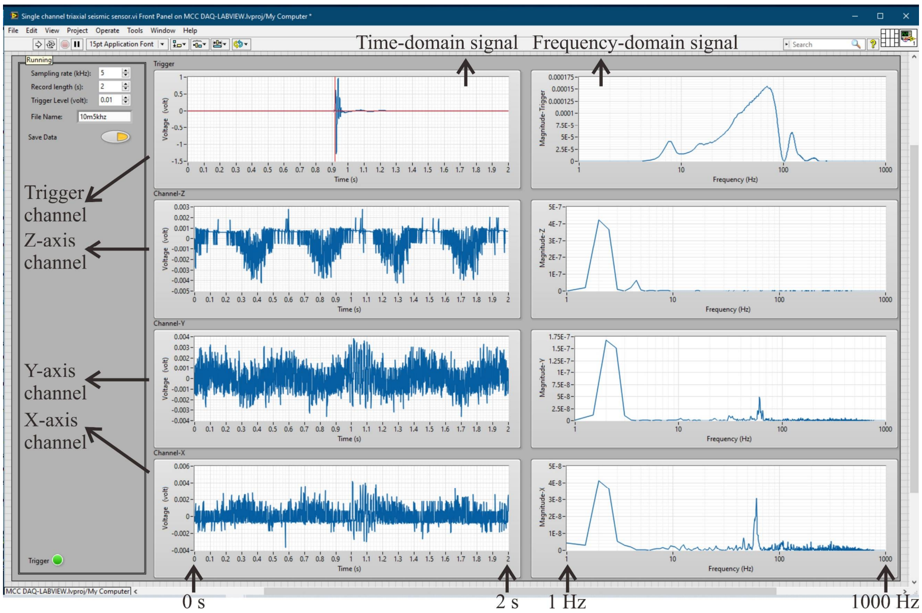

Fig. 8. Displayed signal at 5 kHz sampling rate with 10 m intervals.

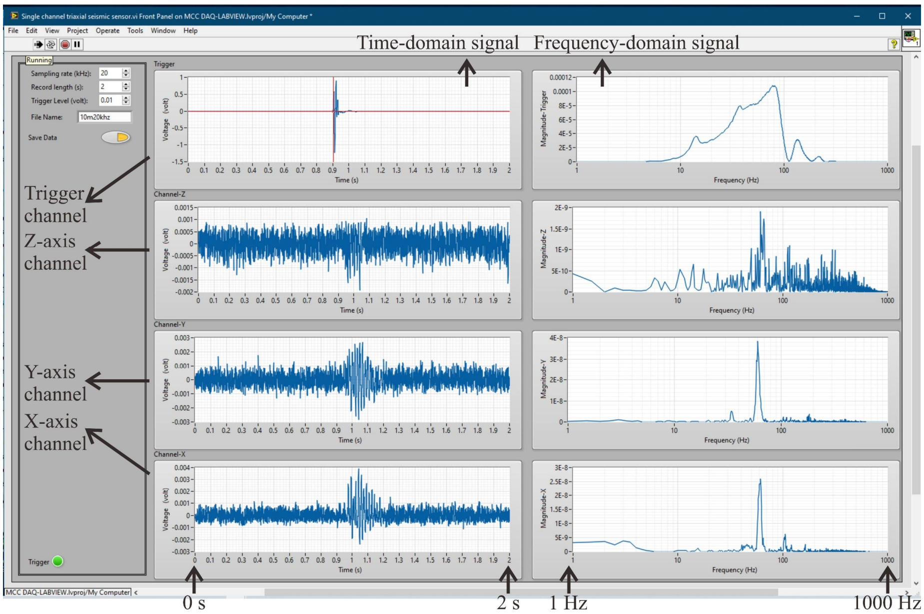

Fig. 9. Displayed signal at 20 kHz sampling rate with 10 m intervals.

Conversely, as the distance between the sensors and the seismic source increases, the recorded signals become distorted and noisy, as illustrated in Figs. 8 and 9 depict ground acceleration at a distance of 10 m. The ground movements exhibit more explicit results when sampled at a rate of 20 kHz. Subsequently, the signals from each axis and sampling frequency are once again overlapped to examine finer details, as shown in Fig. 10. However, the signals cannot be adequately sampled at a frequency of 1 kHz for all channels (X-, Y-, and Z-axis), despite the ground motion frequency being around and below 100 Hz (as seen in the right images of Figs. 8 and 9). According to Nyquist frequency principles, a sampling rate of 1 kHz should suffice, but the desired signal may not be accurately captured in noisy environmental conditions. To address this matter, it is suggested that an appropriate analog filter circuit be incorporated into the sensor's output. However, in this study, the author deliberately omitted the filter to assess the impact of the sampling rate and its effectiveness in the presence of noisy wave signals.

Moreover, the wave displayed in the Z-direction cannot be adequately reconstructed at a sampling frequency of 5 kHz, as depicted in the top image of Fig. 8. This is because the signal is refracted or reflected before being sensed by the Z-axis sensor, resulting in more significant attenuation compared to the ground motions directly detected by the X- and Y-axis sensors. Consequently, the wave's amplitude is significantly weakened, posing challenges for sampling, particularly in noisy conditions. However, between 10 and 25 kHz, the wave signals are sufficiently reconstructed for all channels in any direction, as shown for 20 kHz in Fig. 10.

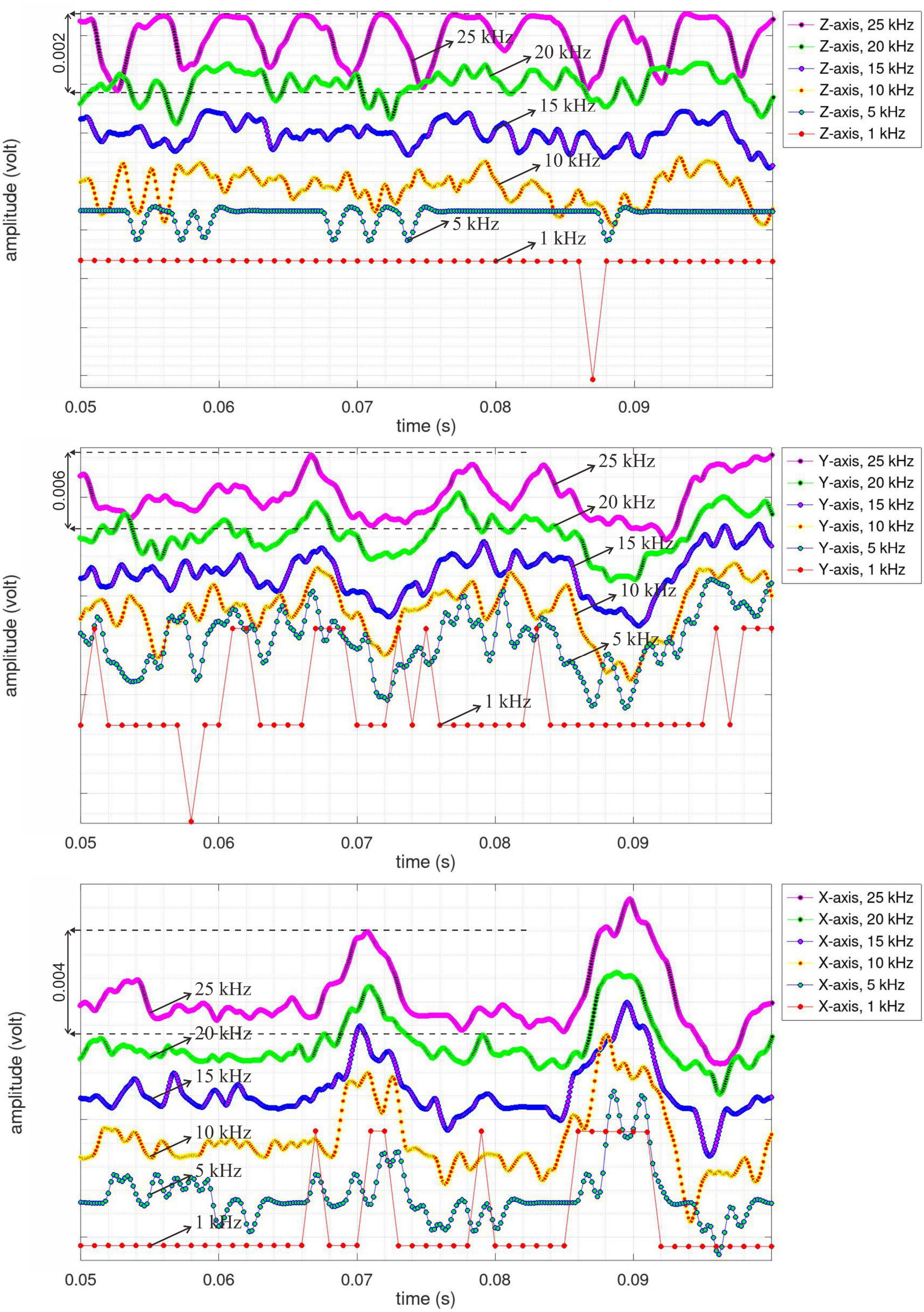

Fig. 10. Signal at a distance of 10 m with disparate sampling frequencies, (top) Z-axis, (middle) Y-axis, and (bottom) X-axis.

Objectives have been achieved from the view depicted in Figs. 5-6 and 8-9; however, further analyses are necessary to ensure their signals are appropriately reconstructed. Fig. 11 illustrates the attenuation curve across all channels as the ground acceleration detected diminishes with increasing distance. The Z-axis exhibits the lowest amplitude compared to the other axes, consistent with the earlier argument. This difference can be attributed to the X-axis (radial) sensing direct waves from the source through the ground surface, as indicated by the measurement setup in Fig. 2(a) and the sensor configuration in Fig. 4. Consequently, the X-axis acceleration shows a higher amplitude. On the other hand, the Y-axis (transversal direction), perpendicular to the direction of ground wave propagation, records the highest amplitude, particularly capturing ground shear and surface waves like the love wave [37].

Figs. 12-14 depict the recorded ground waves across all channels and distances, sampled at a rate of 20 kHz. These images delineate wave arrivals up to 6 m from the source, marked by their initial amplitude occurrences. However, beyond 6 m, noise obscures the detection of the first wave appearances. Additionally, these figures demonstrate that longer distances between the sensor and the wave source result in increased wave travel time. In signal processing, noise can often be mitigated through filtering techniques. Figs. 15-17 exemplify the application of a second-order low-pass filter, resulting in more evident wave traces than the unfiltered data. These findings indicate that the developed system effectively portrays ground wave propagation.

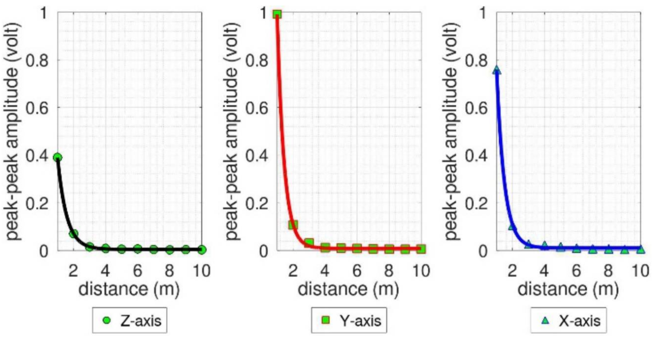

Fig. 11. Curves of signal attenuation: Z-axis (left), Y-axis (middle), and X-axis (right).

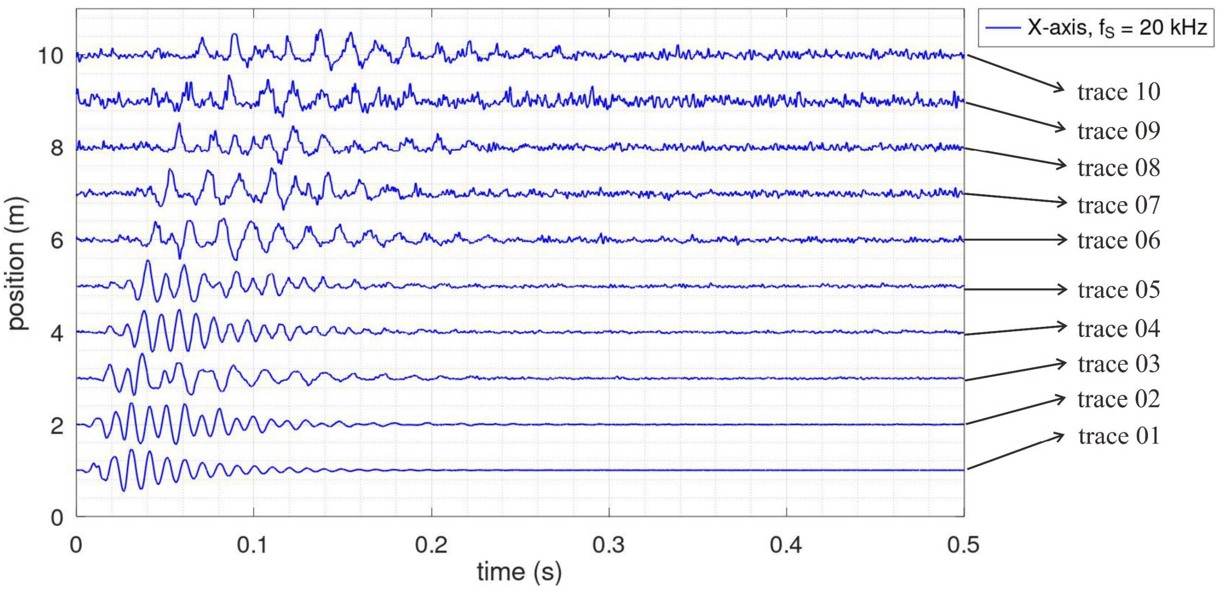

Fig. 12. X-axis wave reconstruction for all distances.

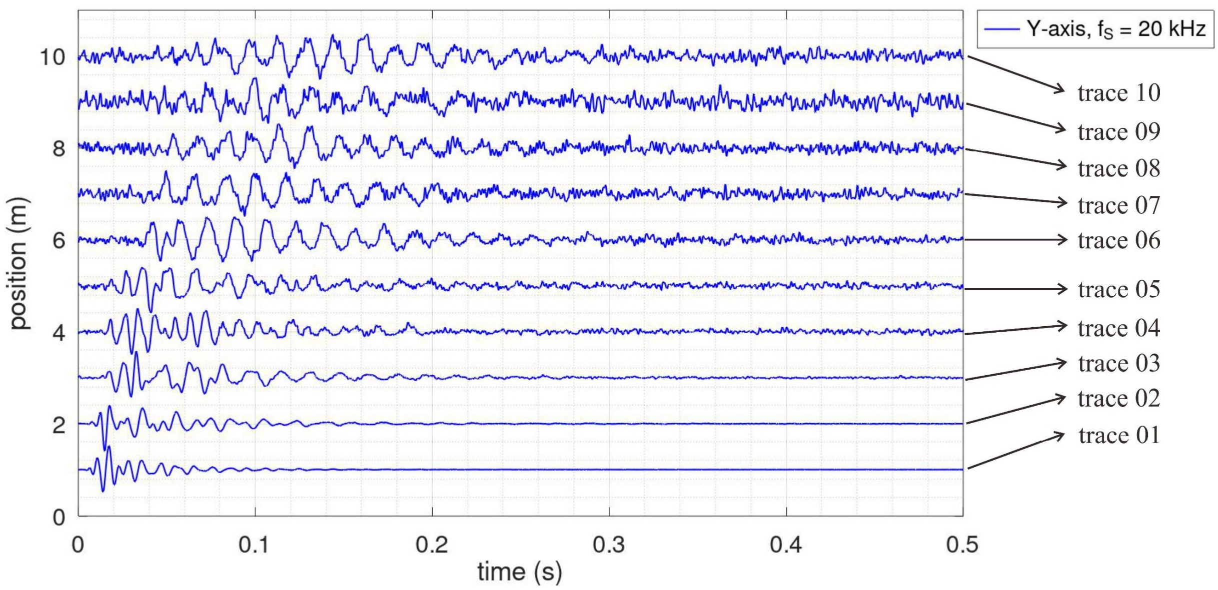

Fig. 13. Y-axis wave reconstruction for all distances.

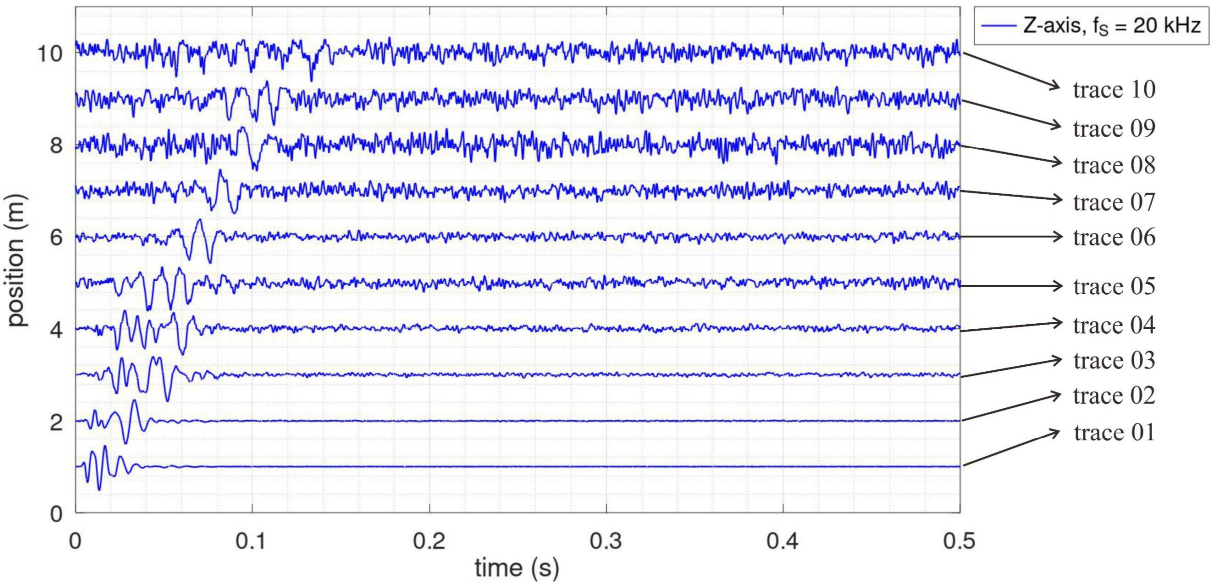

Fig. 14. Z-axis wave reconstruction for all distances.

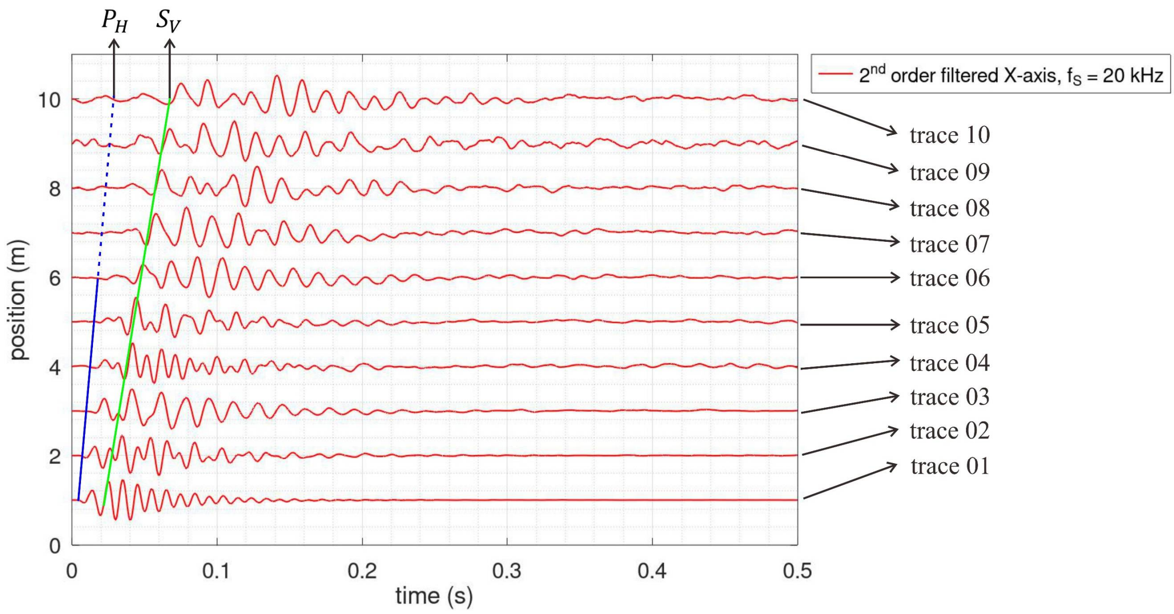

Fig. 15. X-axis waves filtered by processing software.

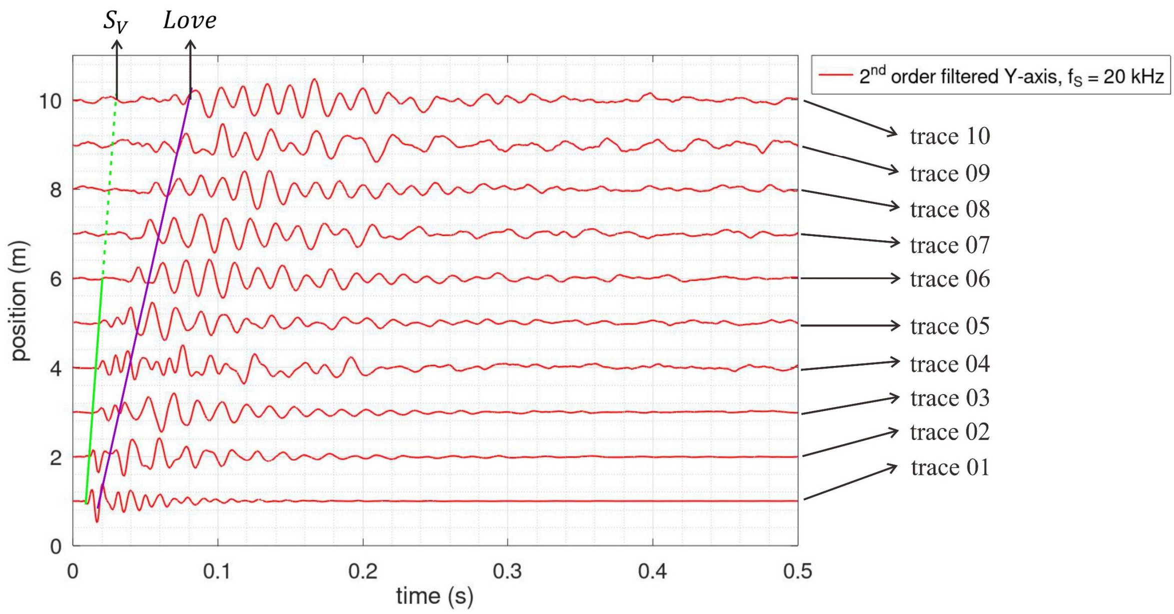

Fig. 16. Y-axis waves filtered by processing software.

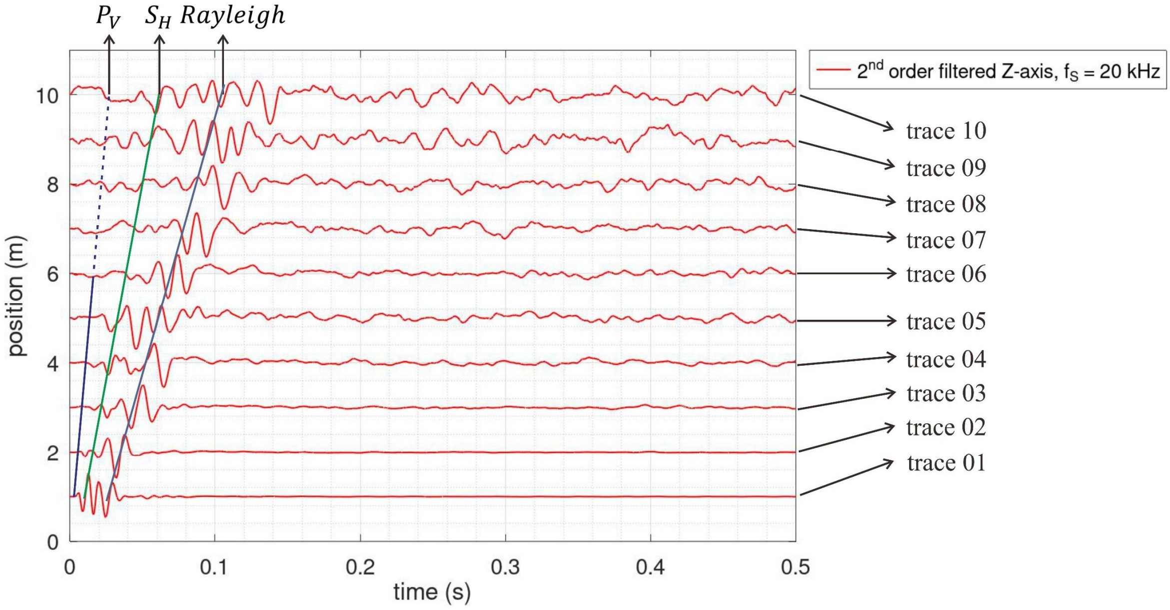

Fig. 17. Z-axis waves filtered by processing software.

Additionally, the spectrum frequency of all traces for each axis is superimposed. Examining these traces in Figs. 18-20 reveals a dominant frequency of approximately 60 Hz, likely from a power line interference present during data acquisition. Beyond this, the frequency responses generally remain under 150 Hz. Notably, in the transversal direction, there's a significant amplitude around 30 Hz, potentially corresponding to the love wave, further supporting the assertion that the Y-axis exhibits the highest amplitude.

Different wave types present in the ground are discernible from the filtered traces (Figs. 15 to 17), encompassing body waves (pressure and shear) and surface waves (Love and Rayleigh). The radial axis captures direct horizontal pressure (P_H) waves followed by vertical shear (S_V) waves, likely resulting from refraction or reflection. Similarly, the transversal sensor detects shear (S_V) waves followed by love waves (Lv). In the Z-axis, vertical pressure waves (caused by seismic wave refraction/reflection) are recorded (P_V), succeeded by horizontal shear (S_H) and Rayleigh (Ry) waves.

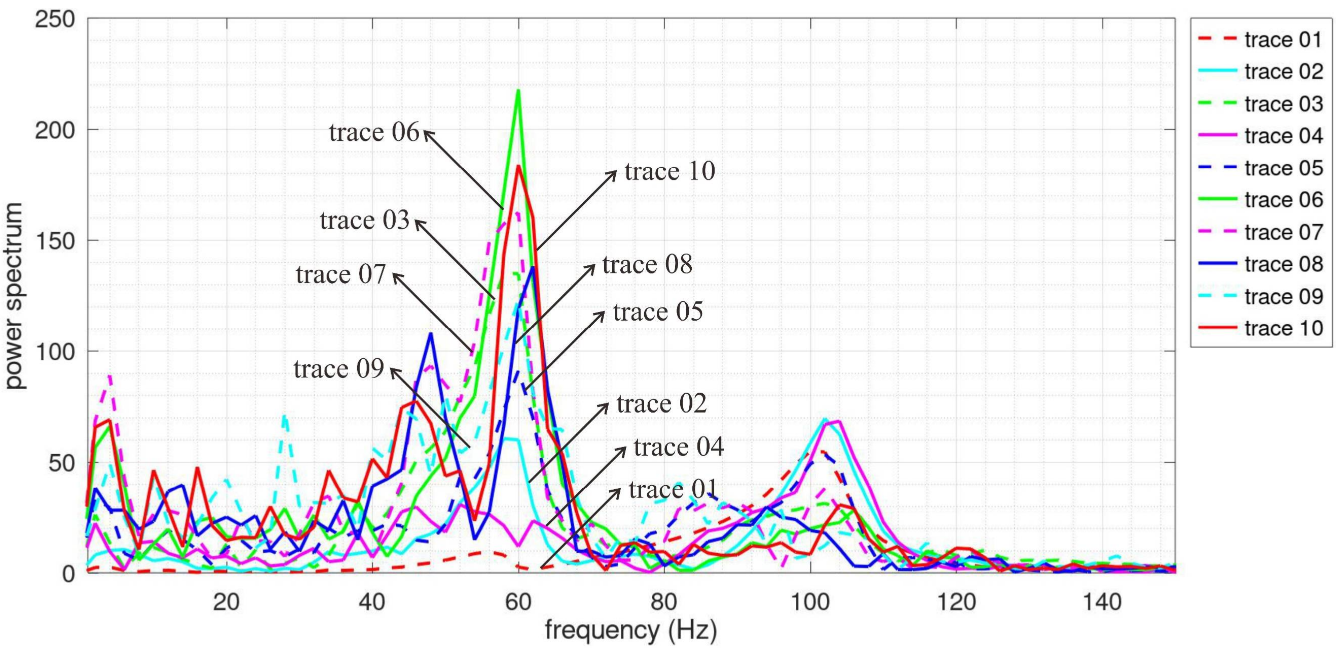

Fig. 18. Spectrum frequency of the X-axis traces.

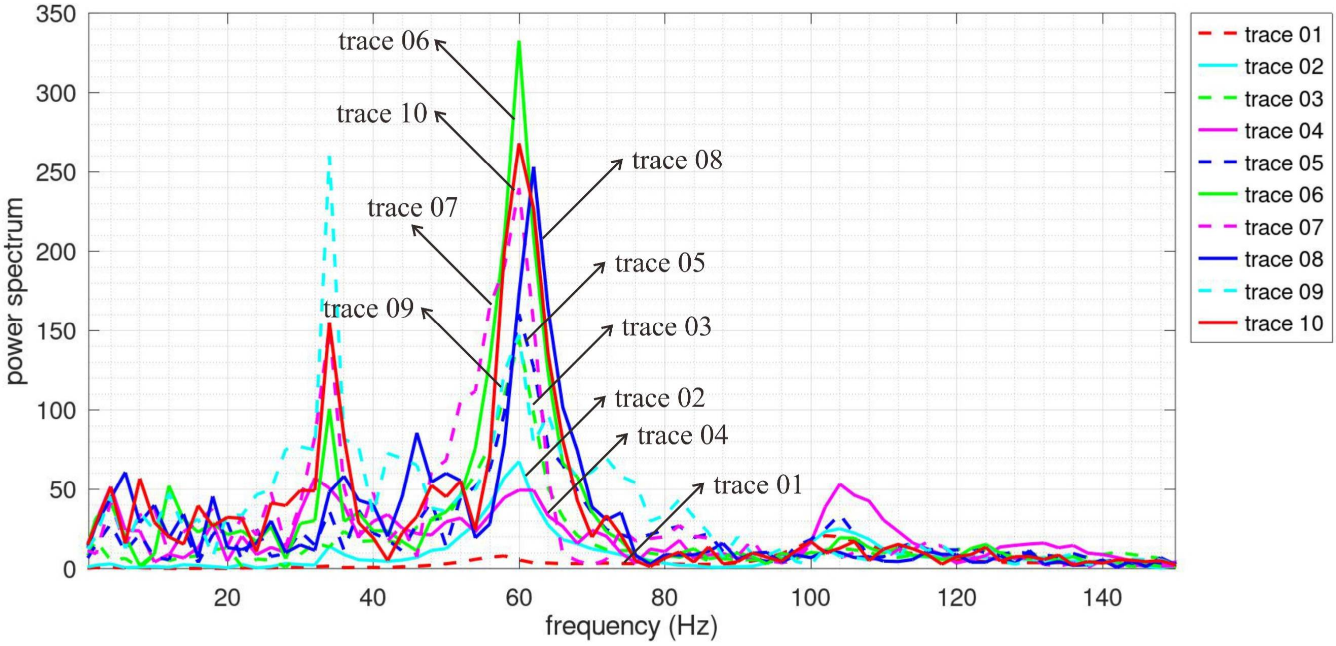

Fig. 19. Spectrum frequency of the Y-axis traces.

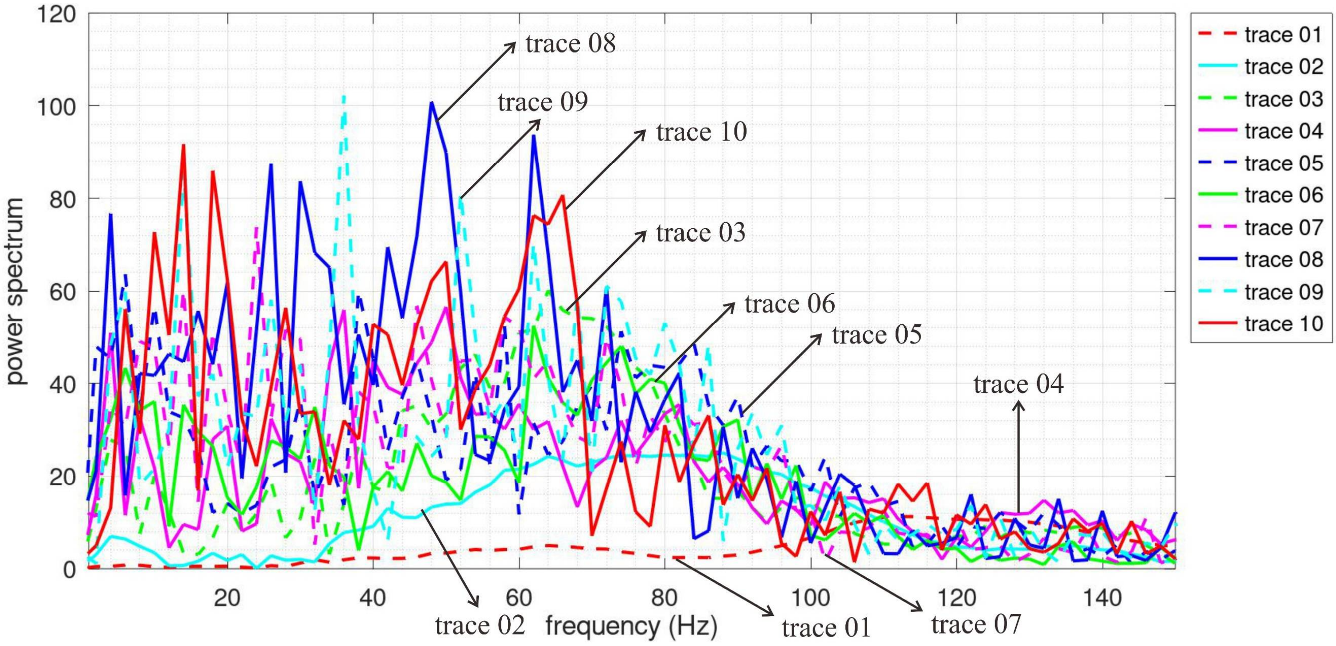

Fig. 20. Spectrum frequency of the Z-axis traces.

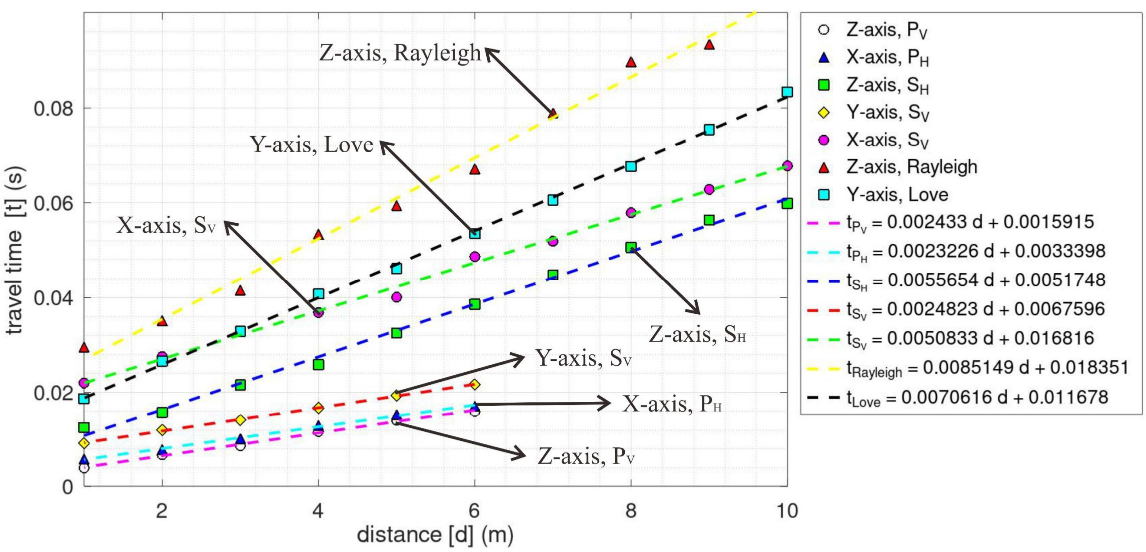

Fig. 21. Waves' travel time.

A simple analysis is conducted to compute wave velocities. Approximation wave arrivals are determined by arranging the first-wave travel times (Figs. 15-17) from each axis up to trace number six (solid line). Their appearances are estimated for subsequent traces based on their higher amplitudes than the preceding wave. Fig. 21 illustrates these wave travel times. Wave velocity is inversely proportional to the slope of each linear curve. Consequently, the ground's wave propagation rates are estimated at 411, 431, 197-403, 180, 142, and 117 m/s for P_V, P_H, S_V, S_H, Lv, and Ry waves, respectively. These values indicate that the sequence of wave velocity is $P_H > P_V > S_V > S_H > Lv > Ry$.

IV. Conclusion

Based on the field test findings, the system employing the LabVIEW programming platform to create graphical software effectively represents ground wave propagation. Its hardware comprises a DAQ and three MEMS accelerometer sensors. The software manages DAQ operations, primarily controlling parameters such as sampling frequency, record length, input channel count, and minimum-maximum input voltage. The software adequately records sensor output and trigger signals connected to DAQ input channels in either time or frequency domains. Sampling frequency plays a crucial role in wave detection, with a sampling rate exceeding 10 kHz proving optimal for reconstructing ground motion despite signal noise.

Several key observations emerge from this study: vertical axis signals experience more significant attenuation compared to other axes; alignment of the seismic source with the horizontal sensor results in another orthogonally flat sensor exhibiting the highest amplitude, possibly indicating the presence of a love wave; and increased spacing between the accelerometer and trigger leads to more extended wave arrival times, consistent with theoretical expectations. Wave arrival times allow for the calculation of wave velocities with P_H wave velocity estimated at around 430 m/s, followed by P_V at 411 m/s, S_V at 197-403 m/s, S_H at 180 m/s, love wave at 142 m/s, and Rayleigh wave at 117 m/s.

Future studies should consider installing analog filter circuits and programmable signal amplifiers in sensor outputs for further system development. Additionally, a comprehensive analysis of outcomes is necessary to characterize ground wave attributes and their relevance to other fields of study.

Acknowledgment

The author extends gratitude to Dr. rer. nat. Rachmat Sule from the Department of Geophysical Engineering, Bandung Institute of Technology, provides MEMS accelerometer sensors.

References

[1] Y. G. Wijaya, N. M. Ula, M. Muksin, and M. G. P. P. Pratama, "Analysis of Vibration in Payload Room Due to Engine Vibration on LSU-05 NG," *Computational And Experimental Research In Materials And Renewable Energy*, vol. 4, no. 1, pp. 21–29, 2021, doi: 10.19184/cerimre.v4i1.24963.

[2] A. K. Desai, A. G. Bharate, V. P. Rane, S. V. Gholap, and A. C. Mitra, "Lab VIEW Programming for Vibration Analysis," *IOSR-JMCE 6th National Conference on "Recent Developments In Mechanical Engineering- 2017"*, vol. 1, 2017, pp. 1–5. doi: 10.9790/1684-17010010105.

[3] Z. A. A. Manjiyani, R. T. Jacob, K. K. R, and B. Varghese, "Development of MEMS Based 3-Axis Accelerometer for Hand Movement Monitoring," *International Journal of Scientific and Research Publications*, vol. 4, no. 2, pp. 1–4, 2014.

[4] M. Yagimli and A. Kaya, "Measurement and Analysis of Drilling Vibration Using Tracer DAQ and LABVIEW," *Journal of Military and Information Science*, vol. 4, no. 2, pp. 45–50, 2016, doi: 10.17858/jmisci.43356.

[5] R. M. Antosia, "Ground Wave Propagation Measurement using DAQ Module and LabVIEW," *International Journal of Computing*, vol. 23, no. 1, pp. 134–143, 2024, doi: 10.47839/ijc.23.1.3445.

[6] S. I. Abdullahi, N. A. C. Mustapha, M. H. Habaebi, and R. Islam, "Accelerometer based structural health monitoring system on the go: Developing monitoring systems with NI LabVIEW," *International Journal of Online and Biomedical Engineering*, vol. 15, no. 7, pp. 32–51, 2019, doi: 10.3991/ijoe.v15i07.10427.

[7] S. Cardona and E. Giraldo, "Real-time Multivariable Embedded Control of a Ball and Plate Prototype," *Engineering Letters*, vol. 29, no. 4, pp. 1375–1380, 2021.

[8] S. Choure and R. H. Adekar, "ARM based 3-Axis Seismic Data Acquisition System using Accelerometer Sensor," *International Journal of Science and Research (IJSR)*, vol. 4, no. 11, pp. 705–708, 2015, doi: 10.21275/v4i11.5111501.

[9] M. A. Mulla, "Hardware Implementation of the Cascaded H-Bridge Inverter using ARM Cortex M4 Microcontroller," *Engineering Letters*, vol. 28, no. 3, pp. 840–847, 2020.

[10] B. López-Castro, A. G. Haro-Baez, D. Arcos-Aviles, M. Barreno-Riera, and B. Landázuri-Avilés, "Systematic Review of Structural Health Monitoring Systems to Strengthen Post-Earthquake Assessment Procedures," *Sensors*, vol. 22, no. 23, p. 9206, 2022, doi: 10.3390/s22239206.

[11] C. G. Juarizo, J. P. Rogelio, J. R. Balbin, and E. P. Dadios, "IoT-Based End-to-End Monitoring of Logistics and Tracking of Truck Vehicles Using Arduino Microcontroller," in *Lecture Notes in Engineering and Computer Science*, 2019, pp. 95–100.

[12] J. He and J. Xia, "Design of a Configurable Remote Data Acquisition System," in *7th International Conference on Energy and Environmental Protection*, 2018, pp. 1744–1748. doi: 10.2991/iceep-18.2018.317.

[13] K. Listewnik, G. Grzeczka, M. Kłaczynski, and W. Cioch, "Real-Time LabVIEW application for diagnostics and evaluation of machine vibration," *Vibroengineering Procedia*, vol. 6, pp. 104–108, 2015.

[14] N. M. N. Al-Dosary, "Development of a LabVIEW Application for Measurement and Analysis of Acceleration Signals from an External Reference," *Journal of Agriculture Science and Technology A*, vol. 7, no. 5, pp. 317–333, 2017, doi: 10.17265/2161-6256/2017.05.004.

[15] A. D'Alessandro, A. Costanzo, C. Ladina, F. Buongiorno, M. Cattaneo, S. Falcone, C. La Piana, S. Marzorati, S. Scudero, G. Vitale, S. Stramondo, and C. Doglioni, "Urban Seismic Networks, Structural Health and Cultural Heritage Monitoring: The National Earthquakes Observatory (INGV, Italy) Experience," *Frontiers in Built Environment*, vol. 5, p. 127, 2019, doi: 10.3389/fbuil.2019.00127.

[16] A. D'Alessandro, S. Scudero, G. Vitale, A. Di Benedetto, and G. Lo Bosco, "Optimization of Low-Cost Monitoring Systems for On-Site Earthquake Early-Warning of Critical Infrastructures," in *Lecture Notes in Computer Science*, vol. 12250, 2020, pp. 963–975. doi: 10.1007/978-3-030-58802-1_69.

[17] A. G. Özcebe, A. Tiganescu, E. Ozer, C. Negulescu, J. J. Galiana-Merino, E. Tubaldi, D. Toma-Danila, S. Molina, A. Kharazian, F. Bozzoni, B. Borzi, and S. F. Balan, "Raspberry Shake-Based Rapid Structural Identification of Existing Buildings Subject to Earthquake Ground Motion: The Case Study of Bucharest," *Sensors*, vol. 22, no. 13, p. 4787, 2022, doi: 10.3390/s22134787.

[18] R. M. Azzara, M. Girardi, V. Iafolla, D. M. Lucchesi, C. Padovani, and D. Pellegrini, "Ambient Vibrations of Age-old Masonry Towers: Results of Long-term Dynamic Monitoring in the Historic Centre of Lucca," *International Journal of Architectural Heritage*, vol. 15, no. 1, pp. 5–21, 2021, doi: 10.1080/15583058.2019.1695155.

[19] E. Barbin, A. Koleda, T. Nesterenko, and S. Vtorushin, "Three-axis MEMS accelerometer for structural inspection," in *Journal of Physics: Conference Series*, vol. 671, 2016, p. 012003. doi: 10.1088/1742-6596/671/1/012003.

[20] P. Ragam and N. D. Sahebraoji, "Application of MEMS-based accelerometer wireless sensor systems for monitoring of blast-induced ground vibration and structural health: a review," *IET Wireless Sensor Systems*, vol. 9, no. 3, pp. 103–109, 2019. doi: 10.1049/iet-wss.2018.5099.

[21] N. Adamo, N. Al-Ansari, V. Sissakian, J. Laue, and S. Knutsson, “Dam Safety: Use of Seismic Monitoring Instrumentation in Dams,” *Journal of Earth Sciences and Geotechnical Engineering*, vol. 11, no. 1, pp. 203–247, 2021, doi: 10.47260/jesge/1116.
[22] K. Fuławka, P. Mertuszka, M. Szumny, L. Stolecki, and K. Szczerbiński, "Application of MEMS-Based Accelerometers for Near-Field Monitoring of Blasting-Induced Seismicity," *Minerals*, vol. 12, no. 5, p. 533, 2022, doi: 10.3390/min12050533.
[23] P. Pierleoni, S. Marzorati, C. Ladina, S. Raggiunto, A. Belli, L. Palma, M. Cattaneo, and S. Valenti, "Performance Evaluation of a Low-Cost Sensing Unit for Seismic Applications: Field Testing during Seismic Events of 2016-2017 in Central Italy," *IEEE Sensors Journal*, vol. 18, no. 16, pp. 6644–6659, 2018, doi: 10.1109/JSEN.2018.2850065.
[24] H. F. Liu, Z. C. Luo, Z. K. Hu, S. Q. Yang, L. C. Tu, Z. B. Zhou, and M. Kraft., "A review of high-performance MEMS sensors for resource exploration and geophysical applications," *Petroleum Science*, vol. 19, no. 6, pp. 2631–2648, 2022, doi: 10.1016/j.petsci.2022.06.005.
[25] M. H. M. Khir, A. Kumar, and W. I. W. Yusoff, "Accelerometer Sensor Specifications to Predict Hydrocarbon Using Passive Seismic Technique," *Journal of Sensors*, vol. 2016, p. 4378540, 2016. doi: 10.1155/2016/4378540.
[26] A. Mercier, C. Dupuis, and B. Giroux, "Geophysical Open Seismic Hardware: Design of a Vertical Seismic Profiling Instrument," *Journal of Open Hardware*, vol. 7, no. 1, p. 3, 2023, doi: 10.5334/joh.50.
[27] D. Mougenot and N. Thorburn, "MEMS-based 3C accelerometers for land seismic acquisition: Is it time?," *The Leading Edge*, vol. 23, no. 3, pp. 246–250, 2004, doi: 10.1190/1.1690897.
[28] A. C. Nur'aidha, D. R. Santoso, and S. Maryanto, "Development of Seismic Data Acquisition Based on MEMS Accelerometer MMA7361L," *International Journal of Applied Engineering Research*, vol. 13, no. 10, pp. 7926–7931, 2018.
[29] R. M. Antosia, R. Sule, and T. Setiawan, "Development of Seismic Data Acquisition Systems in Indonesia," in *Proceedings of the 11th SEGJ International Symposium, Yokohama, Japan*, 2013, pp. 15–18. doi: 10.1190/segj112013-005.
[30] A. C. Nur'aidha, S. Maryanto, and D. R. Santoso, "Implementation of MEMS accelerometer for velocity-based seismic sensor," in *5th International Conference on Electrical Engineering, Computer Science and Informatics (EECSI)*, 2018, pp. 657–662. doi: 10.1109/EECSI.2018.8752918.
[31] A. Chen, F. Cheng, D. Wu, and X. Tang, "Ground vibration propagation and attenuation of vibrating compaction," *Journal of Vibroengineering*, vol. 21, no. 5, pp. 1342–1352, 2019, doi: 10.21595/jve.2019.20388.
[32] A. H. Mohammad, N. A. Yusoff, A. Madun, S. A. A. Tajudin, M. N. H. Zahari, T. N. T. Chik, N. A. Rahman, and Y. M. N. Annuar, "Ground Vibration Attenuation Measurement using Triaxial and Single Axis Accelerometers," in *Journal of Physics: Conference Series*, vol. 995, 2018, p. 012113. doi: 10.1088/1742-6596/995/1/012113.
[33] K. R. Czech and W. Gosk, "Measurement of Surface Vibration Accelerations Propagated in the Environment," in *Procedia Engineering*, vol. 189, 2017, pp. 45–50. doi: 10.1016/j.proeng.2017.05.008.
[34] J. Ramakrishnan, P. T. R. Gaurav, N. S. Chandar, and N. M. Sudharsan, "Structural design, analysis and DOE of MEMS-based capacitive accelerometer for automotive airbag application," *Microsystem Technologies*, vol. 27, no. 3, pp. 763–777, 2021, doi: 10.1007/s00542-020-04979-3.
[35] Colibrys, “SF1500S.A-SF1500SN.A / Single axis best in class seismic accelerometer," 2023, p. 1. Accessed: Apr. 01, 2023. [Online]. Available: https://e2e.ti.com/cfs-file/__key/communityserver-discussions-components-files/73/Colibrys-SF1500-Accelerometer.pdf
[36] MCC, "USB-201 Analog and Digital I/O User's Guide," 2019, p. 14. Accessed: Mar. 06, 2024. [Online]. Available: https://files.digilent.com/manuals/USB-201.pdf
[37] G. Dal Moro, R. Ponta, and R. Mauro, "Unconventional optimized surface wave acquisition and analysis: Comparative tests in a perilagoon area," *Journal of Applied Geophysics*, vol. 114, pp. 158–167, 2015, doi: 10.1016/j.jappgeo.2014.12.016.

Risky Martin Antosia earned a bachelor's degree in Instrumentation Physics and a master's degree in Geophysical Engineering, both from the Bandung Institute of Technology, Indonesia. Since 2019, he has been a lecturer at the Department of Geophysical Engineering, Sumatera Institute of Technology, Indonesia. His academic pursuits focus on instrumentation, computation, and geophysics.